Physics in Medicine & Biology

IPEM Institute of Physics and Engineering in Medicine

PAPER • OPEN ACCESS

Characterization of a multi-pinhole molecular breast tomosynthesis scanner

To cite this article: Beien Wang *et al* 2020 *Phys. Med. Biol.* **65** 195010

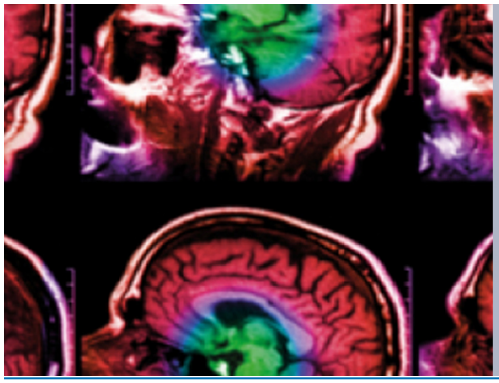

IOP Publishing Phys. Med. Biol. 65 (2020) 195010 https://doi.org/10.1088/1361-6560/ab9eff

Physics in Medicine & Biology

IPEM Institute of Physics and Engineering in Medicine

OPEN ACCESS

RECEIVED
15 January 2020

REVISED
15 June 2020

ACCEPTED FOR PUBLICATION
22 June 2020

PUBLISHED
7 October 2020

PAPER

Characterization of a multi-pinhole molecular breast tomosynthesis scanner

Beien Wang[1], **Jarno van Roosmalen**[1], **Rob Kreuger**[1], **Jan Huizenga**[1], **Freek J Beekman**[1,2,3] **and Marlies C Goorden**[1]

[1] Section of Biomedical Imaging, Department of Radiation Science and Technology, Delft University of Technology, Mekelweg 15 2629 JB, Delft, The Netherlands
[2] MILabs B.V., Heidelberglaan 100 3584 CX, Utrecht, The Netherlands
[3] Department of Translational Neuroscience, Brain Center Rudolf Magnus, University Medical Center Utrecht, Universiteitsweg 100 3584 CG, Utrecht, The Netherlands

E-mail: b.wang-1@tudelft.nl

Keywords: breast imaging, SPECT, gamma camera, pinhole collimator

Abstract

In recent years, breast imaging using radiolabelled molecules has attracted significant interest. Our group has proposed a multi-pinhole molecular breast tomosynthesis (MP-MBT) scanner to obtain 3D functional molecular breast images at high resolutions. After conducting extensive optimisation studies using simulations, we here present a first prototype of MP-MBT and evaluate its performance using physical phantoms. The MP-MBT design is based on two opposing gamma cameras that can image a lightly compressed pendant breast. Each gamma camera consists of a 250×150 mm^2 detector equipped with a collimator with multiple pinholes focusing on a line. The NaI(Tl) gamma detector is a customised design with 3.5 mm intrinsic spatial resolution and high spatial linearity near the edges due to a novel light-guide geometry and the use of square PMTs. A volume-of-interest is scanned by translating the collimator and gamma detector together in a sequence that optimises count yield from the scan region. Derenzo phantom images showed that the system can reach 3.5 mm resolution for a clinically realistic ^{99m}Tc activity concentration in an 11-minute scan, while in breast phantoms the smallest spheres visible were 6 mm in diameter for the same scan time. To conclude, the experimental results of the novel MP-MBT scanner showed that the setup had sub-centimetre breast tumour detection capability which might facilitate 3D molecular breast cancer imaging in the future.

1. Introduction

Breast cancer is the most commonly diagnosed cancer in women. About 25% of cancer diagnoses and 15% of cancer deaths in females are due to breast cancer (Ferlay *et al* 2015). X-ray mammography (sometimes assisted by ultrasound or magnetic resonance imaging) is the most widely-used imaging modality in breast cancer diagnosis (Calonge *et al* 2010). Although x-ray mammography has generally high diagnostic sensitivity (over 80%) and reasonably low dose (less than 1 mSv), it suffers from a reduced sensitivity (as low as 30%–50%) for patients with dense breasts, which is especially disadvantageous as dense breasts (typically defined as >50% dense tissue in breast) are associated with higher cancer risk (Yaffe 2008, Berg 2009). For example, women with >75% dense tissue in breasts may have an over 4 times higher risk of getting breast cancer than women with <10% dense tissue in breasts (Boyd *et al* 2007).

Recently, dedicated molecular breast imaging using radiolabelled tracers has been applied in a clinical setting and has been proven to provide diagnostic information complementary to that of conventional x-ray mammography, especially for patients with dense breasts (Hruska and O'Connor 2013, Rechtman *et al* 2014, Rhodes *et al* 2015). Several planar breast scintigraphy devices (Hruska *et al* 2012a, 2012b, Siman and Kappadath 2012, Long *et al* 2016), dedicated breast SPECT (Brzymialkiewicz *et al* 2005, Gong and Williams 2015, Gilland *et al* 2017) and PET (Macdonald *et al* 2009, Baghaei *et al* 2010, Yanagida *et al* 2010, Moliner

et al 2012) scanners are under development or available from manufacturers. These dedicated systems are preferred over whole-body general-purpose scanners, as they improved count yield and resolution in the breast.

So far, molecular breast imaging has mainly been applied as a supplementary imaging tool for patients whose mammograms did not provide sufficient diagnostic information (Shermis *et al* 2016). Its application as a general screening tool would require a reduction in dose, which is currently about 10 mSv for ^{99m}Tc-Sestamibi (Hendrick 2010), the only FDA-approved single photon emitting tracer that can be use in breast imaging, though the possibility of imaging with lower dose (less than 3 mSv) is under investigation (Kuhn *et al* 2016, Long *et al* 2016). As many tracers assessing physiological processes such as blood flow, glucose consumption, aberrant cellular proliferation, gene/protein expression associated with cancer, lipid metabolism, and tumour hypoxia are available or under development (Specht and Mankoff 2012), molecular imaging may not only have diagnostic applications but could also play a role in developing individualised treatment plans or in monitoring therapy.

Recently, our group proposed a novel multi-pinhole molecular breast tomosynthesis (MP-MBT) scanner dedicated to image the 3D distribution of single gamma-emitting tracers in the breast (Beekman 2015, van Roosmalen *et al* 2016), with the aim to detect small breast tumours which are conventionally hard to detect in dense breasts (Russo *et al* 2016, Hruska *et al* 2008b). In the MP-MBT design (figure 1), the patient lies prone on a bed containing a hole for the breast which is slightly compressed by two transparent plates. Two webcams placed behind the compression plates view the breast and their images serve as input to a graphical user interface on which the user can select a scan region (Branderhorst *et al* 2011). The breast is then scanned by translating two gamma cameras (gamma detector equipped with focusing multi-pinhole collimator) over a sequence of positions. Due to the focusing pinhole geometry and the possibility to confine the scan region, the scanner has the option to focus on a small suspect region in order to increase count yield from that region. An accurate 3D imaging capability such as offered by MP-MBT can be beneficial in diagnosis as, compared to 2D images, it reduces tissue pile-up which may obscure a tumour (Brzymialkiewicz *et al* 2005, Gilland *et al* 2017). Furthermore, 3D images can provide information on the depth and shape of the tumour. Currently, the commercially available planar breast scintigraphy devices image a breast in two perspectives (craniocaudal and mediolateral oblique views) to determine the tumour's position in the depth dimension (Hruska *et al* 2012b, Long *et al* 2016).

In previous simulation studies, we have designed and optimised the MP-MBT system (van Roosmalen *et al* 2016, 2017, 2018) and its image reconstruction (Wang *et al* 2017). The optimisation aimed to obtain the best ^{99m}Tc-Sestamibi image, however, other ^{99m}Tc-labelled tracers under investigation (Spanu *et al* 2011, O'Connor *et al* 2017) and may also be imaged with the same design. Additionally, we built and characterised a gamma detector specifically designed for this application (Wang *et al* 2018, 2019). Based on these previous studies, we have now built a prototype scanner to experimentally characterise the concept of MP-MBT. To evaluate the performance of the prototype scanner, we performed phantom experiments using a customised Derenzo resolution phantom as well as a customised breast phantom. In this paper, we describe the newly built MP-MBT setup and present the phantom scan results.

2. Methods

The built prototype setup contains a dedicated gamma detector with a multi-pinhole collimator (SAM Precision B.V.) mounted in front, an XYZ linear module (GaoGong ChuanDong Co., Ltd.) to translate the gamma camera (0.03 mm precision according to manufacturer's specifications), and a table in front of the gamma camera with a hole in it to imitate the patient bed (figure 2). In the designed geometry, two gamma cameras view the breast from opposite directions. As we currently have only one gamma camera available, we emulate the two-camera imaging procedure by scanning the phantom from one side, rotating it by 180° (assume it a perfect rotation), and scanning it again from the other side. The equivalent camera-camera distance in the scans is 63 mm (see also figure 1(a)).

2.1. Collimator and detector details

The lead multi-pinhole collimator (figure 1(c)) contains a 6 mm-thick collimator plate with 42 pinholes, as well as a second 10 mm-thick shielding plate with rectangular holes between the collimator and the detector to prevent overlapping of pinhole projections (so-called multiplexing) on the detector. The two plates are attached by four surrounding 3 mm-thick rectangular plates made of lead. The pinholes in the collimator are grouped in 6 rows of 7 pinholes each. The 7 pinholes in each row all focus on a point 40 mm away from the collimator face, with a maximum angle between pinhole axis and direction perpendicular to the collimator of 50° (figure 1(b)). The distance between neighbouring rows of pinholes is 24 mm. Each pinhole has a 2.9 mm diameter and opening angle of 40°. As in this design, the breast is viewed by the pinholes over an

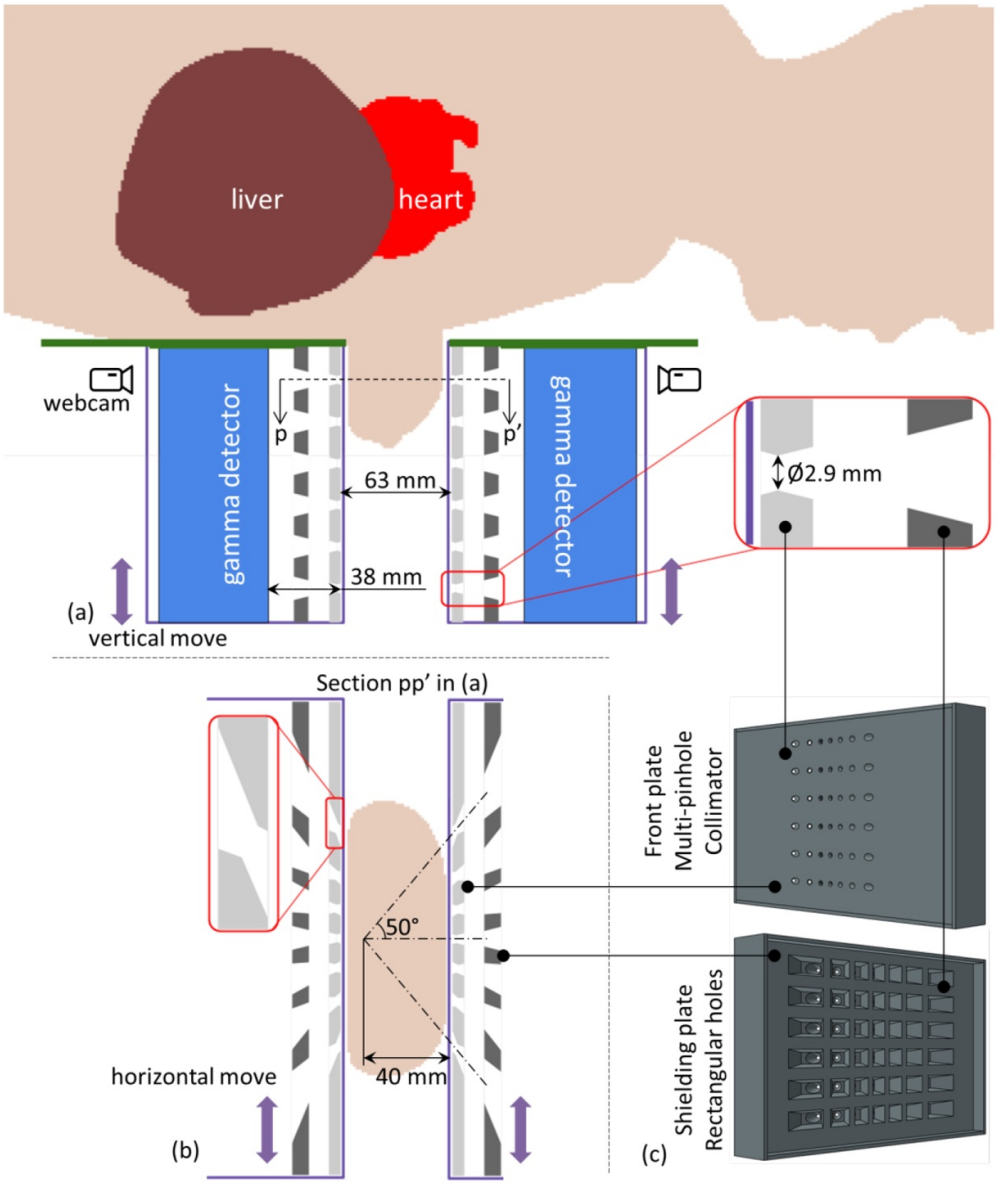

Figure 1. MP-MBT design. (a) A sagittal view of the scanner with the six rows of pinholes and geometry of the system displayed. (b) Coronal view through section pp' in (a) with the focusing geometry of the pinholes shown. (c) The multi-pinhole collimator 3D design showing collimator and shielding plate. The gamma cameras (surrounded by the violet lines) move horizontally and vertically during a scan. The transparent plates for compression are stationary and are not shown in this figure.

angular range less than 180°, the technique is denoted by tomosynthesis instead of tomography. The design criteria for this collimator can be found in van Roosmalen *et al* (2017). The front face of the collimator is placed 38 mm in front of the entrance face of the gamma detector.

A conventional Anger detector was not suitable for this setup because of the large unusable edges (>4 cm) that are commonly present in these types of detectors (Wang *et al* 2018). We, therefore, employ a customised design, comprising a 250 × 150 × 9.5 mm^3 NaI(Tl) scintillator (Scionix B.V.) attached to a 13.3 mm-thick glass light-guide and read out by 15 Hamamatsu R6236 square PMTs with a 56 × 56 mm^2 effective area placed in a staggered layout (see figure 2(b)). The staggered PMT layout is enabled by a novel light-guide design (Wang *et al* 2019): two PMTs at the upper edge of the detector collect the light from the scintillator through two additional light-guides (150 mm long quartz with 60 × 31 mm^2 cross-section, 80% transmission); such a design allows to realise the staggered layout without having to extend these two PMTs outside the scintillator's upper edge where the patient bed is located and thus no space is available. With this novel detector design, facilitated by maximum likelihood interaction position estimation (Barrett *et al* 2009), we are able to obtain high spatial linearity near the detector edges in a cost-effective way as we used rather large PMTs and a continuous scintillator. A maximum likelihood threshold equivalent to a ± 10% energy window was applied (Wang *et al* 2019). The unusable upper edge of gamma detector is about 15 mm

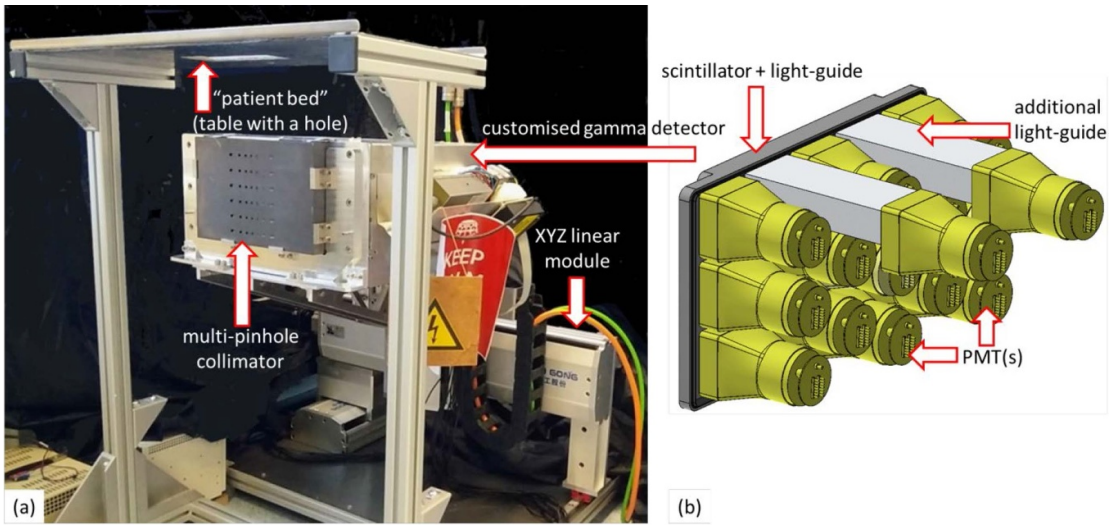

Figure 2. (a) MP-MBT proof-of-concept setup. The customised gamma camera is equipped with a multi-pinhole collimator and placed underneath the table representing the patient bed. It can be translated with a linear XYZ module. (b) A schematic representation of the customised gamma detector showing the encapsulated scintillator and light-guide, as well as two additional light-guides wrapped in reflecting material, and the 15 PMTs (Wang *et al* 2019).

including the 12 mm thick sealing case (made of aluminium) for the scintillator. The average full-width half-maximum (FWHM) spatial resolution for the detector is 3.4 mm and 3.7 mm in horizontal and vertical directions, respectively. A detailed description and more figures of merit characterising the performance of this customised gamma detector were reported in Wang *et al* (2019).

2.2. Point source calibration and system matrix generation

To calibrate the scanner, we measured 522 point spread functions (PSFs) over the field of view by moving the gamma camera in front of a 10 MBq ^{99m}Tc point source of about 1 mm diameter (figure 3(a)), which is the same point source calibration procedure as described in van der Have *et al* (2008) but with different point source positions (due to the different scanner geometries). In total, the calibration measurement took about one hour, which was enough to obtain high-count projections at each position. This measurement was used to obtain the position/orientation deviations of the assembled gamma camera with respect to the designed geometry (CAD drawing of the collimator) similarly to what was done in Goorden *et al* (2016). In this method, it is assumed that the actual collimator-detector geometry is well described by a rotation/translation with respect to the design. Thus, from the calibration, 12 parameters were estimated (3 angles describing the rotation, 3 distances describing the translation, both for the collimator and the detector). The system matrix for image reconstruction was subsequently generated using voxelized raytracing (VRT) software developed in our group (Wang *et al* 2017) with the designed geometry and the geometrical information from the point source calibration as inputs. VRT takes attenuation (in the collimator and the detector) into account but ignores photon scatter. The collimator in VRT was modelled with 1/8 mm voxels of different materials (lead or vacuum) and the detector was modelled by a continuous piece of 9.5 mm thick NaI. The scintillation process and electronic noise of the gamma detector are also not modelled in VRT. Instead, the combined effect is included in the detector intrinsic resolution modelling. The gamma detector intrinsic resolution was set to 3.5 mm FWHM by blurring the VRT-generated PSFs with a 3.5 mm FWHM Gaussian kernel, which was the average value over the whole detector surface obtained by measurements (Wang *et al* 2019). As we had only one gamma camera, we measured the system matrix for this gamma camera and rotated it by 180° to generate the system matrix for the virtually opposite gamma camera. In the current study, we have not corrected for a possible mismatch between the system matrix rotation and the physical phantom rotation. In appendix A.3, a comparison between the measured PSFs and VRT-generated PSFs can be found.

2.3. Phantom acquisitions

To assess the scanner's spatial resolution, a Derenzo phantom (figures 3(b)) printed in our institute (with Formlabs Clear resin), was scanned. The phantom is a cylinder of 50 mm height and 52 mm diameter, with 35 mm long cylindrical rods inside. At each end of the rods, a chamber of 3 mm height and 47 mm diameter facilitates the filling of the phantom. Scans of the phantom with the rods filled with two activity concentration levels (37 kBq ml^{-1} ^{99m}Tc and 370 kBq ml^{-1} ^{99m}Tc) were obtained to evaluate the system resolution. The phantom was placed in the (virtual) centre in between the two gamma cameras during

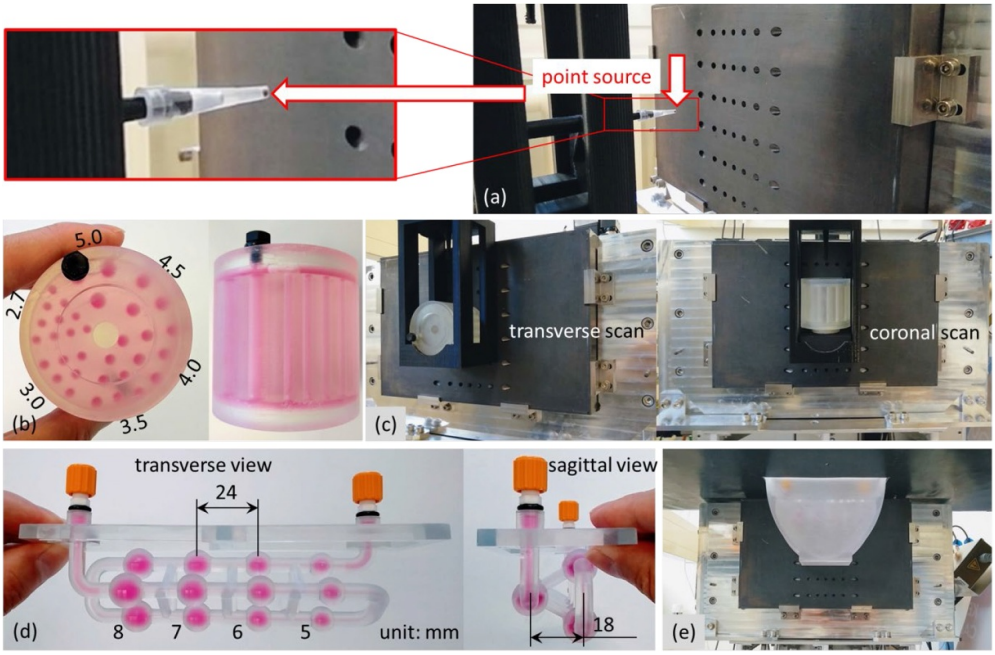

Figure 3. Setup for calibration and phantom measurements. (a) Setup for point source measurement including an enlarged view of the source. (b) The Derenzo phantom with rod diameters indicated (rods were filled with red ink for better visualisation). In each sector the distance between two rods was 2 times the rod diameter. (c) Derenzo phantom measurement setup for horizontal and vertical directions in order to analyse the spatial resolution in transverse and coronal planes. (d) Tumour phantom with the diameters of the spheres and distances between neighbouring spheres indicated (spheres were filled with red ink for better visualisation). (e) Breast phantom measurement setup with the tumour phantom inside. All 3D printed phantoms are water-equivalent under 140 keV gamma radiation.

scanning. To check the spatial resolution in transverse and coronal directions, two scans were performed at each activity concentration with the phantom in two different orientations (figure 3(c)).

Secondly, a breast phantom containing spheres of different sizes, representing different tumours, was scanned. The breast chamber (DSM Somos® Watershed XC 11 122 resin; QingLiu 3D Tech. Co., Ltd.) was 3D printed and has the shape of a semi-elliptic cylinder with 110 mm semi-major axis, 75 mm semi-minor axis, and 55 mm thickness, representing the dimensions of a mildly compressed average breast (figure 3(e)) (Hruska and O'Connor 2008a, Gilland *et al* 2017). The tumour phantom (3D Systems Accura® 60 resin; Phantech LLC.) was also 3D printed and contains three sets of 8 mm, 7 mm, 6 mm, and 5 mm diameter spheres connected by channels with 1 mm inner diameter (figure 3(d)). The neighbouring spheres in each set have a 24 mm separation, and all spheres are at a distance of 22.5 mm and 40.5 mm from the two collimator plates. The ^{99m}Tc activity concentration injected into the tumour phantom was 37 kBq ml^{-1} while the breast phantom was filled with a background activity concentration of 3.7 kBq ml^{-1}. These levels represent a realistic activity concentration in a clinical setting when 925 MBq of ^{99m}Tc-Sestamibi is injected (Maublant *et al* 1996, Hruska and O'Connor 2008a, Mann *et al* 2012). A measurement with a 15 times higher activity concentration was also done as a reference.

Two scanning modes were applied in the phantom experiments; a whole-breast mode and a focusing mode. The whole-breast mode uses a sequence of gamma camera positions in a step-and-shoot way that is suitable to scan the entire breast; in this case, the gamma camera moves over a 156 mm distance in the horizontal direction and 22.5 mm in the vertical direction (90 scan positions). In the focusing mode, the scan sequence is adapted such that only part of the breast is imaged. In this case, the gamma camera moves 18 mm horizontally around the 5 mm spheres and 22.5 mm vertically (55 scan positions). A description of the specific gamma camera positions in the whole-breast mode and focusing mode can be found in appendix A.1, while the sensitivity maps and volumes-of-interest (VOIs) can be found in appendix A.2. In this study, the whole-breast mode sequence was used in both Derenzo phantom and breast phantom scan, while the focusing mode sequence was used only in the breast phantom scan with the three 5 mm spheres in the focus. In both modes, the total scan time was 11 min (emulated by two 11 min scans at each side). For the breast phantom, we additionally added projections from two 11 min measurements to obtain one emulated 22 min scan. In total, eight 11 min whole-breast mode and focusing mode scans of the breast phantom were performed, and with this dataset four 22 min whole-breast and focusing scans were also obtained.

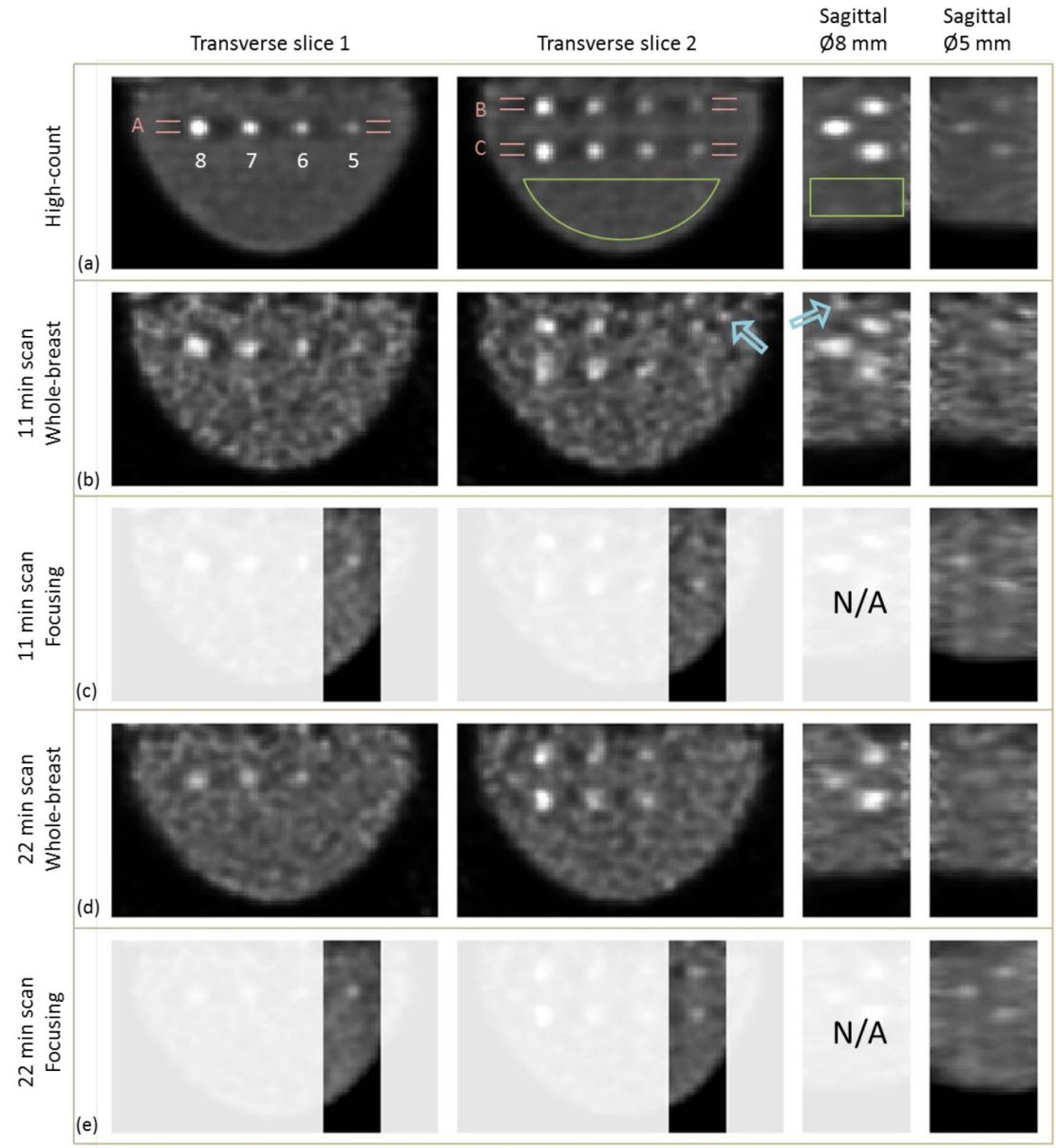

Figure 4. Reconstructed slices of the breast phantom with the tumour phantom inside. (a) High-count scan (550 kBq ml^{-1} injected in the tumour phantom and 55 kBq ml^{-1} injected in the breast phantom) of the breast phantom as a reference image of the phantom. The area with green boundaries refers to the background ROI used to calculate the CNR. (b) 11 min whole-breast scan of the breast phantom and tumour phantom with realistic activity concentration (37 kBq ml^{-1} in tumour phantom and 3.7 kBq ml^{-1} in the background). (c) 11 min scan with realistic activity concentration focusing at the 5 mm spheres. Only the part of reconstructed slices within the focus is shown (therefore the sagittal slice through the 8 mm spheres is dubbed N/A, i.e. Not Available). (d) and (e) 22 min scans in whole-breast and focusing modes. All images have 4.5 mm slice thickness and are taken from 16-iteration MLEM reconstructions, and a 2.0 mm FWHM Gaussian filter is applied for better visualisation.

2.4. Analysis of reconstructed images

All images were reconstructed with a Maximum Likelihood Estimation Maximisation (MLEM) algorithm (Shepp and Vardi 1982). No attenuation or scatter correction was applied. Besides visual inspection of the reconstructed images, we used the tumour-to-background Contrast-to-Noise Ratio (CNR) to evaluate the image quality. The CNR is defined by:

$$\mathrm{CNR} = \frac{\bar{S} - \bar{B}}{\sigma}, \tag{1}$$

where $\bar{S}$ is the average activity in the tumour, $\bar{B}$ denotes the average activity in the background, while σ is the standard deviation of the activity in the background region. The regions-of-interest (ROIs) selected to determine tumour and background activities are shown in figure 4(a). The ROIs are spheres with the same radii as the tumours.

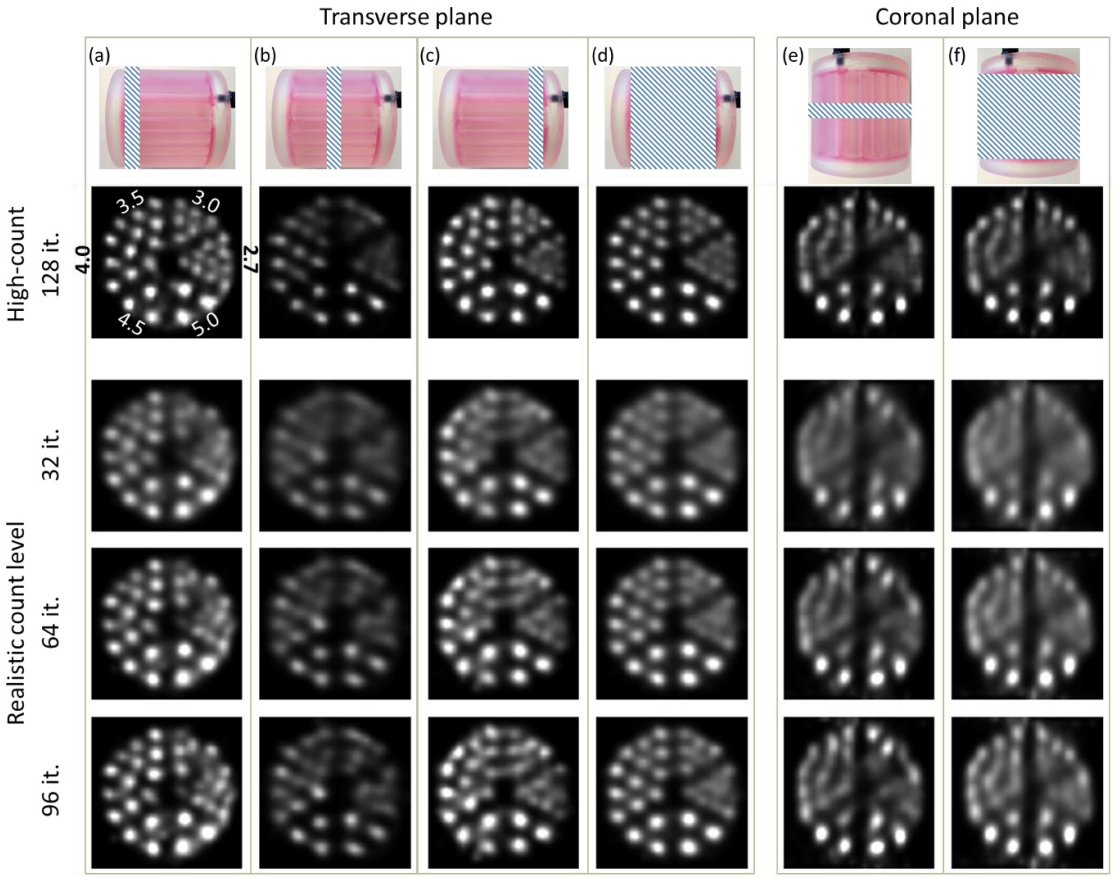

Figure 5. Derenzo phantom images obtained at different iteration numbers. The top row illustrates the location, orientation and thickness of the displayed slices. Gamma camera orientation was in the vertical direction on all images. The second row shows the images obtained with a high activity concentration of 370 kBq ml^{-1} activity (as a reference) while the other rows display images with a realistic 37 kBq ml^{-1} activity concentration obtained at different MLEM iterations filtered with a 2.0 mm FWHM Gaussian kernel for better visualisation. Columns (a)–(c) show transverse slices of 4.5 mm thick taken at the two ends and in the middle of the phantom when it was placed horizontally between the two (virtual) gamma cameras. Column (d) displays a transverse slice of 33 mm thickness. Columns (e) and (f) display coronal slices with 4.5 mm and 33 mm slice thickness obtained from the phantom placed vertically. All realistic count level images were displayed on the same grey scale, the 10 times higher count images were displayed on a ten times larger grey scale.

The tumour phantom includes four sets of 3 spheres of the same size (figure 3(d)). Therefore, the data of 24 spheres were available to determine the mean and standard deviations of the CNR for every tumour size in the 11 min scans, while the data of 12 spheres were used in the 22 min scans.

3. Results

3.1. Derenzo phantom

Figure 5 shows Derenzo phantom images for different slices, slice thicknesses and phantom orientations at several iteration numbers. All images on the same row with the same slice thickness are displayed with the same colour scale. From these images, it can be inferred that in the transverse plane, the spatial resolution is location-dependent: in the centre exactly in-between the two gamma cameras (figure 5(b)), the spatial resolution is poorer than in the regions close to one of the gamma cameras (figures 5(a) and (c)). Such a phenomenon is also observed in the coronal slices in figure 5(e) and (f), in which the upper and lower regions in each image appear clearer than the central part. There is no significant variation along the transaxial direction of the phantom in the coronal scan, therefore, only one slice in the centre of the phantom is shown in the coronal plane (figure 5(e)).

From figures 5(a)–(c), the smallest rods that can be distinguished in the 4.5 mm transverse slices are about 3.0 to 3.5 mm (depending on location) when a realistic 37 kBq ml^{-1} activity concentration is used. When summing all slices (33 mm) together (figure 5(d)), 3.0 mm rods are clearly visible and even 2.7 mm rods can partly be seen. In the reference high-count phantom (filled with 370 kBq ml^{-1} activity), 2.7 mm rods are visible in the 4.5 mm transverse slices near the two ends of the phantom and in the 33 mm thick slices, but in the central part of the phantom, the smallest rods that can be distinguished are 3.5 mm in

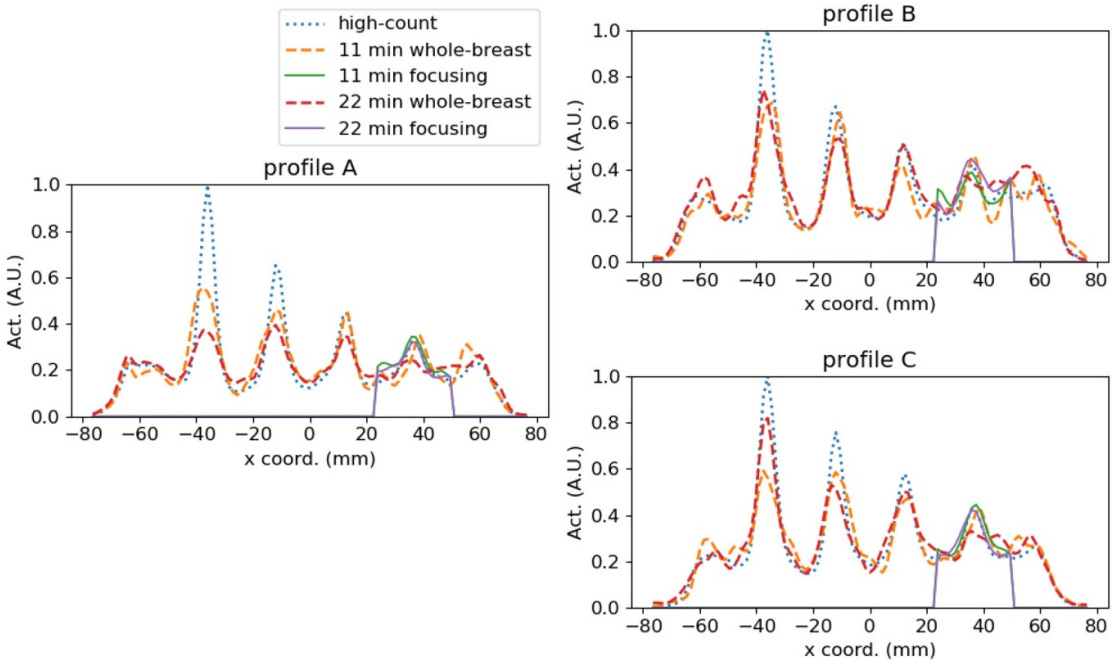

Figure 6. Profiles through tumour phantom from reconstructed slices (as indicated in figure 4(a)). Reconstructed activity in the high-count measurement is divided by 15 (ratio between high-count and realistic activity concentrations), and at each profile, the reconstructed activity is normalised to the high-count measurement's maximum respectively. The tumour-to-background activity concentration ratio was 10:1.

diameter. In the coronal plane, the smallest distinguishable rods are 3.5 mm in diameter regardless of the amount of activity and the slice thickness.

3.2. Breast phantom

Slices through the breast phantom images are displayed in figure 4. In the 11 min whole-breast scan of a breast containing a realistic activity concentration (figure 4(b)), the 8 mm and 7 mm spheres are all clearly visible, while two out of three of the 6 mm spheres are visible. The 5 mm spheres cannot be distinguished from the background at all. It also appears from the images that the background contains noise with spatial correlations, meaning that structures that could be mistaken as lesions are visible (indicated by blue arrows in figure 4(b)). Though buried in background noise in the whole-breast mode scan, the 5 mm spheres can be better distinguished when scanning in the focusing mode (figure 4(c)), both in the transverse and the sagittal slices. For the 22 min scan (figures 4(d) and (e)), the background noise is reduced, which makes the 6 mm spheres better visible in the whole-breast mode, while in the focusing mode, the 5 mm spheres are better resolved than in the 11 min scan. Moreover, in the sagittal view, all spheres are elongated, which indicates that the spatial resolution of the system is different in different directions as is also clear from the Derenzo phantom scans. It is worth noting that the upper edges of the reconstructed volumes close to the chest wall are not displayed as they have artefacts due to the 15 mm unusable edge of the detector (Wang *et al* 2019). We will come back to this point in the discussion section.

To better visualise the results in figure 4, profiles (4.5 mm width; indicated by the red lines in figure 4(a)) through the three rows of tumours are plotted in figure 6 for different scan modes and activity levels. The spheres invisible in figure 4 show up as small 'bumps' in figure 6, but can be hardly distinguished from the background.

Table 1 shows the average CNRs and their standard deviations. In our MP-MBT images, a CNR > 4 usually indicates that the sphere can be easily distinguished from the background, while CNR < 3 indicate that it is impossible to distinguish them, which is comparable to the Rose criterion (1948). The quantitative results in table 1 confirm the visual impression in figures 4 and 6. A complete record of the CNRs from all measurements can be found in appendix A.6.

4. Discussion

In the Derenzo phantom images (figure 5), slices near one of the two gamma cameras appear better resolved than those at the centre exactly in between the cameras. This phenomenon exists regardless of the amount of

Table 1. Average CNR (with standard deviation) of the tumour phantom spheres of different sizes (and scan modes).

diam. (mm) sphere	CNR of 11 min scan	CNR of 22 min scan
8	6.0 ± 1.4	7.9 ± 1.4
7	4.3 ± 1.1	5.6 ± 0.8
6	3.4 ± 1.2	4.5 ± 0.6
5	1.7 ± 1.0	2.4 ± 0.9
5 (focusing)	3.2 ± 0.9	3.8 ± 0.5

activity inside the phantom. We believe that this is due to the geometry of the MP-MBT system in which pinhole magnification factors differ significantly depending on the location in the scanner. From van Roosmalen *et al* (2017), we estimate that system resolution in the slice in between cameras (shown in figure 5(b)) is 6.6 mm, while for the slices close to one of the cameras (figures 5(a) and (c)) better system resolutions of 4.8 mm are calculated. Moreover, reconstructed slices near the centre of the phantom are also lower in intensity than those near the collimator, which is clearly visible in the images in figure 5. We investigated this issue by doing a full simulation of the Derenzo phantom scan (with/without attenuation, with/without detector blur, and with/without noise) using our VRT software. From the simulations, we found that for noise-free projections, the central slice attains a similar intensity and spatial resolution as the more peripheral slices only after thousands of MLEM iterations, i.e. the central part of the image converges slower than the peripheral parts which is to be expected given the larger PSF FWHM. However, if we reconstruct the experimental images with more iterations, the noise in the reconstructed images increases which degrades visual image quality even if a post-filter is applied and therefore, we chose to show images at an intermediate number of iterations. Attenuation of the gamma rays in the Derenzo phantom plays only a minor role here. A more complete analysis of this non-uniform spatial resolution and intensity issue is provided in appendix A.4.

In the images shown in figure 4(b) and (d), the presence of spatially correlated noise is the main reason that the 5 mm spheres are not well visible. The pattern of the noise is very similar in appearance to small lesions, which may cause false-positive diagnoses (blue arrows in figure 4(b)). Such a noise pattern was also visible in our earlier simulation study for different collimators (van Roosmalen *et al* 2018). However, in the high-count measurement (figure 4(a)), the noise pattern is largely reduced. Moreover, such a noise pattern is not commonly visible in low-sensitivity clinical or preclinical SPECT images (complete sampling over 180°), which may suggest that the observed noise pattern results from the interplay between limited count statistics and sampling incompleteness. The cause of the pattern is still under investigation, but we provided a further analysis based on simulations in appendix A.5.

To overcome the correlated noise issue and increase the specificity of MP-MBT for smaller tumours, the use of a longer acquisition time might be a solution, as has been shown by the improvement of images in figures 4(d) and (e). Although only mild breast compression is applied, for longer measurements, the comfort of patients may be impaired, and risk of motion artefacts increases. Therefore, it could be impractical to increase acquisition time. Currently, the overhead time of the camera movement is about 10% of the total acquisition time. In the future if this overhead can be further minimised by, for instance, (i) a list-mode acquisition with continuous gamma camera motion or (ii) a faster linear module, we would expect a slight improvement in image quality. Another solution may be to use a different reconstruction algorithm. Instead of MLEM without any prior information, a maximum *a posteriori* reconstruction (Nuyts *et al* 2005) for general purpose SPECT or PET and total variation reconstruction (Velikina *et al* 2007) for x-ray breast tomosynthesis are reported to lead to improved noise characteristics. A post-filter other than the current Gaussian filter may also change the noise appearance in the reconstructed image. Therefore, further investigation of different reconstruction algorithms and post-filters for MP-MBT could be a subject of future research.

The whole-breast mode of MP-MBT could be used to search for any lesions in the breast at the diagnostic stage, while the focusing mode could be performed after a tumour is detected using the whole-breast mode or by another modality, to better determine its shape, to confirm if a tumour was successfully treated, or to further characterise the tumour, possibly by using different tracers simultaneously (Zhou *et al* 2012, Elvas *et al* 2015, Josefsson *et al* 2016, Deken *et al* 2019, Solomon *et al* 2019). In this aspect the method can have advantages over PET since SPECT has the unique ability to perform multi-isotope imaging. Compared with planar breast scintigraphy devices, MP-MBT gives extra information on the 3rd dimension which is useful in determining the location, size and shape of the tumour and which may increase tumour-to-background contrast.

The current gamma detector has a 15 mm dead edge of which 12 mm is due to the sealing material. Discussions with manufacturers have indicated that it is probable that the sealing of the scintillator can be made more compact (possibly as small as 5 mm) so that this dead edge can likely be significantly reduced in the future. On the other hand, in the current study, we did not take the required thickness of the patient bed into account. In Wang *et al* (2017), we concluded that about 3 mm lead is needed for the patient bed to shield the torso activity. Considering the steel frame of the bed and the cushion (compressed), this will at least add another 5 mm of effective dead edge. To deal with the dead edge issue, we are also considering a collimator design with pinholes pointing a bit towards the patient's chest which would allow us to better image the chest area.

Compared with other molecular breast tomosynthesis/tomography scanners which mostly utilise parallel hole collimators or variable slant hole collimators (Brzymialkiewicz *et al* 2005, Gong *et al* 2015, Gilland *et al* 2017), our system has the special property of being able to focus on a pre-defined area. It is not easy to compare the whole-breast mode of different systems, as different studies use different activity concentrations, scan times, and phantoms. Here we discuss different design choices made when developing these scanners. Gilland *et al* (2017), Gong *et al* (2015) and our system apply mild compression of the breast, while Brzymialkiewicz *et al* (2005) did not apply any compression and the breast was freely pendant. As a result, in the former three systems, the gamma camera can be placed very close to the breast during scanning which generally increases the resolution-sensitivity trade-off, while in the latter system the gamma camera can move freely around the breast to obtain complete angular sampling, i.e. fully 3D tomography instead of tomosynthesis. Both scanners described in Gilland *et al* (2017) and Gong and Williams (2015) use a geometry with the patient standing upright which is the same as in commercially available planar breast scintigraphy devices (Hruska 2017), which allowed for integration of a biopsy module similar to that of existing planar systems (Long *et al* 2016). Our present version of the system images a prone patient and an image guided biopsy could possibly be taken in between the two compression plates or by using compression plates that contains holes (Beekman 2009) in combination with shifting a camera and collimator aside. Integrating a biopsy module into our scanner could be a future direction of upgrading the design.

5. Conclusion

To conclude, our group has built a setup to test the concept of MP-MBT. Using a Derenzo phantom we showed that the system's spatial resolution was about 3.5 mm, while a breast phantom scan showed the smallest detectable tumours to be 6 mm in the whole-breast mode and 5 mm in the focusing mode for a clinically realistic activity concentration and tumour-to-background uptake ratio of 10:1. Therefore detection of tumours close to a half centimetre may be possible with the MP-MBT system, though challenges related to reducing the correlated background noise remain. MP-MBT might be a supplementary tool to standard x-ray mammography or x-ray breast tomosynthesis in diagnosing breast cancers because of its many unique imaging capabilities e.g. for characterising tissue.

Acknowledgments

We thank Benjamin Cox and Justin Jeffery from Phantech LLC. for designing and printing the tumour phantom. We thank Malte Verleg and Kevin Kamman from DEMO at TU Delft for designing and printing the Derenzo phantom, and the former also for all the help in the mechanical aspect of MP-MBT. We thank Kathalijne de Nijs, Daan van der Ham and Jason Mulder for their work on the optimisation of several aspects of MP-MBT. This work is supported by the Dutch Organization for Scientific Research (NWO) under the VIDI grant 12371 'Focused imaging of tumors'.

Appendix

A.1. Scan sequences. The scan sequences can be found in figure A1.

A.2. Sensitivity maps and VOIs for different scan sequences

In figure A2, the sensitivity maps together with the field of view of a stationary collimator position and the selected VOIs for the two scan modes in the paper are shown. The areas displayed in figure A2 are the same as those displayed in figure 4. The width of VOI in the focusing mode (width of the orange boxes in the coronal and transverse view in figure A2(c)) is 27 mm. The peak sensitivities and differential uniformities (standard deviation of sensitivity divided by the mean sensitivity) in the VOIs of the system are provided in table A1.

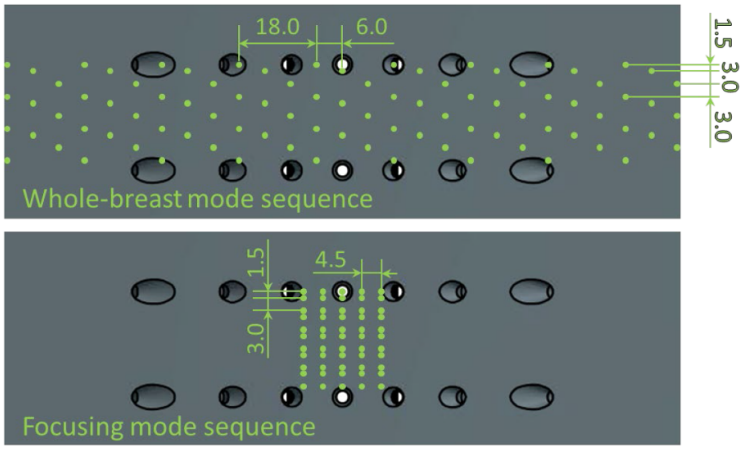

Figure A1. The sequences of the two scan modes used in MP-MBT with respect to the multi-pinhole collimator. For the whole-breast mode, the neighbouring scanned positions have a 18 mm interval, while there is a 6 mm horizontal shift between neighbouring rows; the vertical neighbouring rows have a 1.5 mm or 3.0 mm interval. For the focusing mode, the horizontal interval is fixed at 4.5 mm, while the vertical interval is either 1.5 mm or 3.0 mm.

Table A1. Sensitivity and uniformity.

	Peak sensitivity	Uniformity over VOI
Stationary position	0.75%	–
Whole-breast mode	0.082%	33%
Focusing mode	0.37%	37%

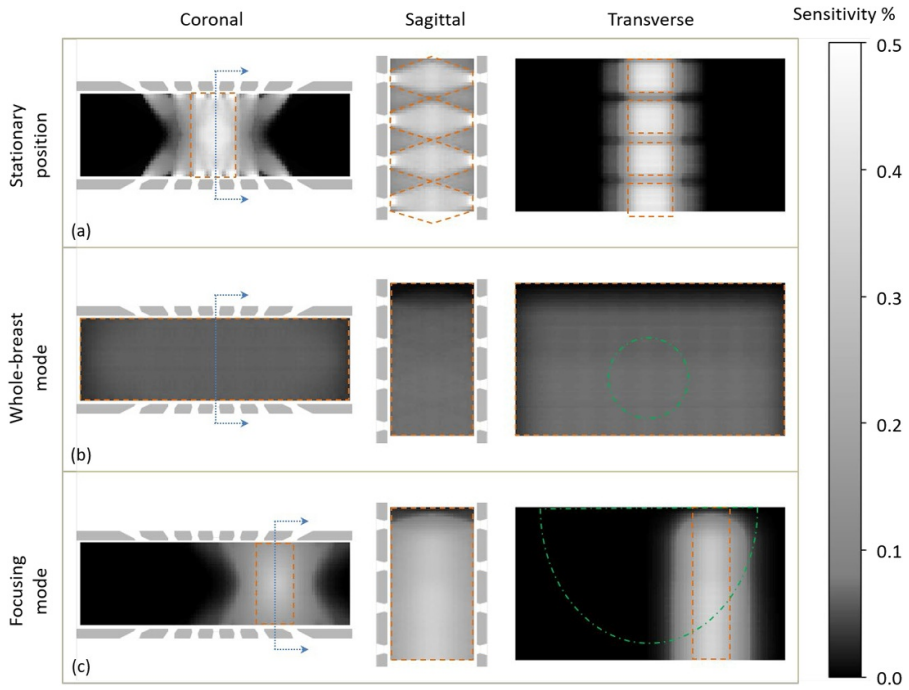

Figure A2. The sensitivity map of MP-MBT in the stationary position and for two scan sequences with the multi-pinhole collimator shown. The sagittal and transverse areas shown here are the same as in figure 4. The sagittal sections are taken from the blue dotted line shown in the corresponding coronal sections, and the transverse sections are all taken exactly in between two gamma cameras in the coronal section. The field of view of the stationary position and the VOIs of the two scan modes are marked in orange. The size of the Derenzo phantom and the breast phantom are marked green in the transverse view.

A.3. Comparison of measured and simulated (VRT-generated) PSFs

In figure A3, a comparison of PSFs at three different positions is shown. Beside these three positions, we also calculated the root mean square errors (RMSE) between the measured PSFs and VRT-generated PSFs for all

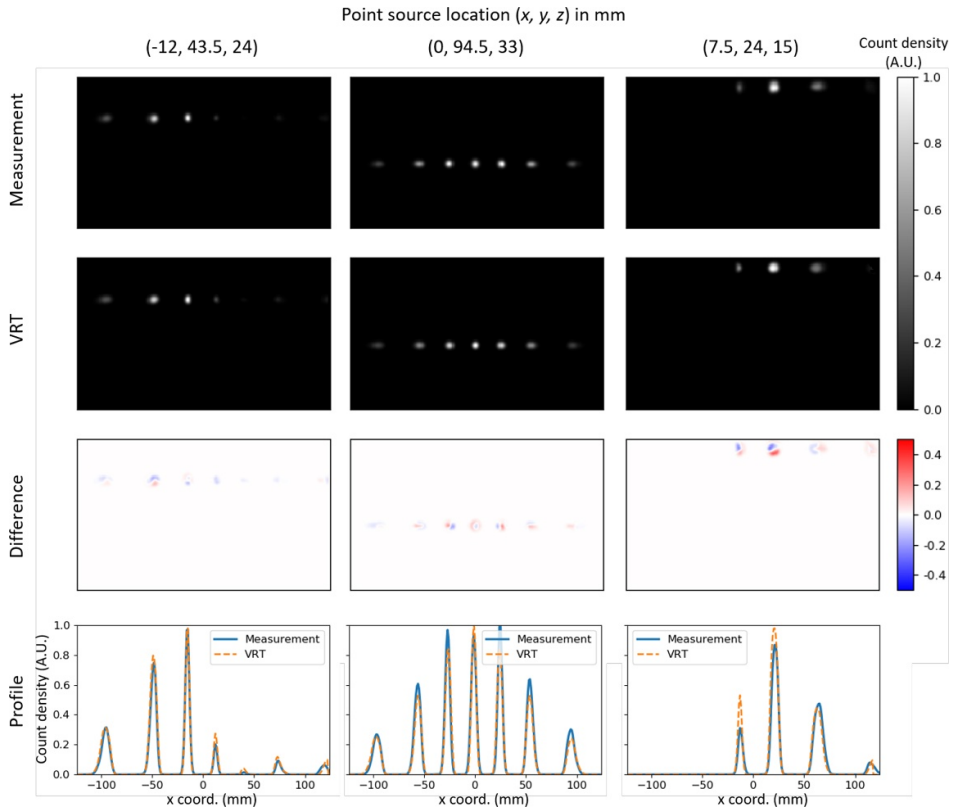

Figure A3. Comparison of measured and VRT-generated PSFs at three example positions (the three columns). The projection images in the first row are measured PSFs, while the projection images in the second row are VRT-generated PSFs at the same position. The first row subtracted by the second row is shown in the third row. The fourth row provides profiles through the PSFs.

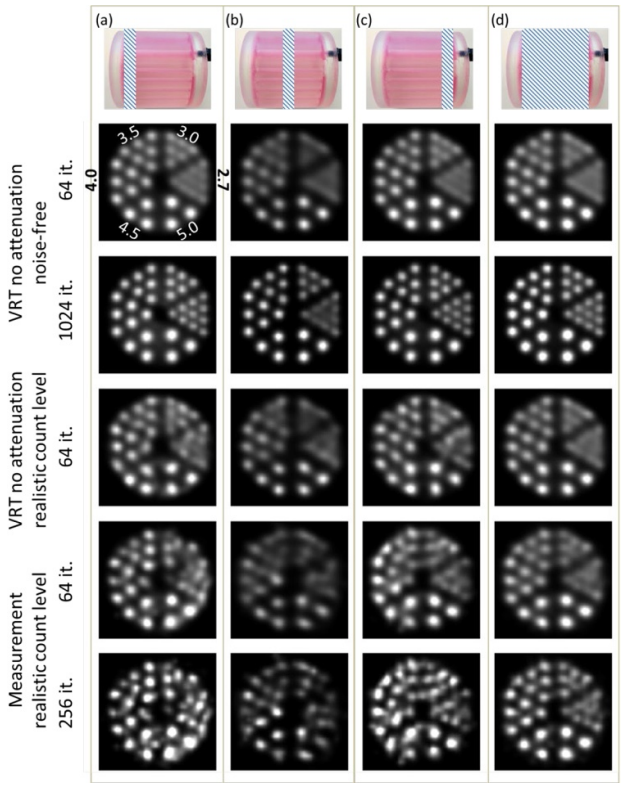

Figure A4. The reconstructed slices (transverse scan) of a horizontally placed Derenzo phantom obtained from VRT simulated and measured projection data. Image processing of all reconstructions is done in the same way as in figure 5 and the activity concentration in the realistic count level reconstructions is the same for VRT-simulated data and measurements.

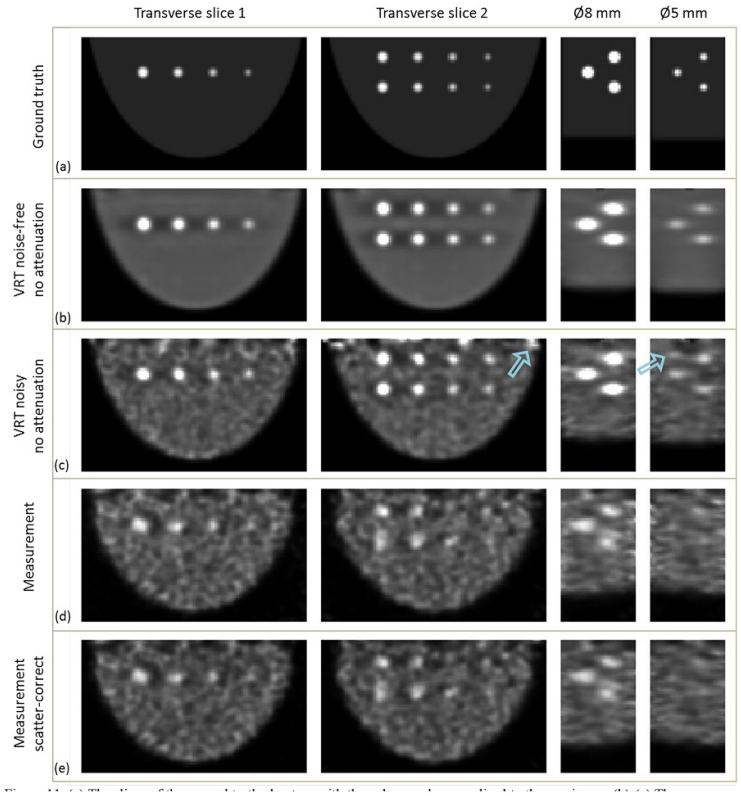

Figure A5. The slices (a) of the ground truth phantom with the colour scale normalised to the maximum. (b)-(e) The reconstructed slices of the breast phantom with the tumour phantom inside from VRT simulation and measurement. The image processing of the ground truth phantom and all the reconstructions is the same as in the 11 min scans in figure 4. The activity concentration in the VRT noisy data is the same as in the measurement data. The side energy windows used in the TEW scatter correction in (e) are at 126 keV and 154 keV with ± 14 keV width. All images have 4.5 mm slice thickness. (b)-(e) are taken from 16-iteration MLEM reconstructions, and a 2.0 mm FWHM Gaussian filter is applied for better visualisation.

Table A2. CNRs of the tumour phantom spheres of different sizes from the 11 min scans.

		Whole breast, tumour diam.				Focusing, tumour diam.
Measurement	Row	8 mm	7 mm	6 mm	5 mm	5 mm
	A	7.55	6.41	5.02	3.29	4.00
1	B	5.97	4.91	2.67	3.61	1.75
	C	5.23	5.56	3.79	2.78	4.29
	A	5.94	3.52	1.13	1.78	2.52
2	B	6.40	4.21	4.08	2.69	2.82
	C	6.59	4.58	2.62	0.90	3.20
	A	4.26	3.88	3.80	1.01	2.62
3	B	5.58	4.35	5.66	1.32	2.17
	C	7.61	4.40	2.39	0.62	2.79
	A	7.10	4.50	2.74	2.90	4.16
4	B	4.83	2.26	2.77	2.19	3.20
	C	4.71	4.45	6.44	2.68	4.96
	A	4.92	4.52	3.30	1.19	3.27
5	B	6.44	1.12	3.28	0.27	1.97
	C	7.41	4.94	3.13	0.91	3.59
	A	3.33	3.21	2.28	0.53	3.24
6	B	5.82	6.07	3.23	0.94	5.36
	C	7.96	3.49	5.25	0.82	3.52
	A	4.92	3.79	3.57	1.27	2.39
7	B	7.17	5.01	2.85	0.33	2.14
	C	5.40	5.17	3.06	1.44	2.70
	A	3.45	3.56	2.35	1.53	3.30
8	B	7.20	3.98	2.77	2.51	3.99
	C	8.73	5.31	4.02	2.74	2.47

Table A3. CNRs of the tumour phantom spheres of different sizes from the 22 min scans.

Measurement	Row	Whole breast, tumour diam.				Focusing, tumour diam.
		8 mm	7 mm	6 mm	5 mm	5 mm
1	A	7.47	5.46	4.48	3.05	4.59
	B	6.92	4.32	5.04	3.00	3.27
	C	7.90	5.96	5.50	2.52	4.71
2	A	9.15	6.03	3.95	3.15	3.62
	B	8.10	5.71	4.43	4.20	3.44
	C	7.79	6.70	4.59	2.37	3.64
3	A	5.72	5.26	3.78	1.57	4.10
	B	8.15	4.57	4.32	0.88	4.09
	C	10.22	5.79	5.48	1.26	4.19
4	A	5.30	4.82	3.92	1.42	3.57
	B	9.00	6.00	3.67	2.58	3.61
	C	9.22	7.03	4.56	2.97	3.15

522 measured positions. The definition of RMSE is:

$$\mathrm{RMSE}_{\mathrm{Meas.,VRT}} = \sqrt{\frac{\sum_{n=1}^{N_{\text{over thres.}}} \left(I_{\mathrm{Meas.}}(n) - I_{\mathrm{VRT}}(n)\right)^2}{N_{\text{over thres.}}}}, \tag{A1}$$

where $I_{\mathrm{Meas.}}(n)$ and $I_{\mathrm{VRT}}(n)$ are the pixel values in measured and VRT-generated projection image at pixel index n (normalised to each image's maximum), $N_{\text{over thres.}}$ is the number of pixels over a 1% (of the image maximum) threshold in the VRT-generated projection image. The average RMSE over the 522 positions is 6.1%.

A.4. Investigation of the cause of non-uniform spatial resolution

In figure A4, we show a few VRT-simulated Derenzo phantom reconstructions and compare these with the measurement to investigate the non-uniform spatial resolution phenomenon mentioned in the Discussion. As can be seen in the 64-iteration reconstructed images, no matter if there is attenuation, scatter, geometry mismatch (which there possibly is between VRT and measurement), or noise, we find poorer spatial resolution in the central slice of the phantom than at the edges (figure A4(b)). However, if we increase the iteration number to 1024 MLEM iterations, the noise-free images from VRT-simulated projections give almost the same spatial resolution over the phantom. A 256-iteration number reconstruction of the measured data is shown in the last row of figure A4, and it already looks very distorted. Thus, we choose to only use a moderate number of iterations for reconstructing the measured data.

A.5. Investigation of the cause of spatially correlated noise

In figure A5, we show a few VRT-simulated breast phantom (with tumour phantom insert) reconstructions and compare these with the measurements to investigate the spatially-correlated noise artefacts mentioned in the Discussion. As can be seen in figure A5(b), we do not see any correlated patterns in the noise-free images. The measured high-count images in figure 4(a) show stronger artefacts than the noise-free reconstruction but less artefacts than the simulated realistic count level images. Moreover, in the images of the noisy VRT-generated projections (no attenuation or scatter) in figure A5(c), with no mismatch between the system matrix and the projection images except for Poisson noise, the artefacts still exist (all though less than in the measurement). Therefore, we conclude that the spatially correlated noise depends on the number of counts. In our experience, systems with complete angular sampling do not show such strong artefacts even for low count levels. Therefore, we think that sampling incompleteness is also relevant here. An additional reconstruction with a triple energy window (TEW) scatter correction (Ogawa *et al* 1991) of the measurement data in figure A5(e) showed no improvement compared with figure A5(d), which provides the same reconstruction but without scatter correction. Therefore, we did not apply scatter correction in all reconstructions and concluded that scatter correction does not solve the artefacts.

A.6. Complete list of the CNRs from all measurements

Calculated CNRs from all our 11 min and 22 min measurements are listed in tables A2 and A3 respectively. In the tables, 'Row' refers to the rows marked in pink in figure 4.

ORCID iDs

Beien Wang https://orcid.org/0000-0002-0893-2641
Jarno van Roosmalen https://orcid.org/0000-0001-7043-2587

References

Baghaei H, Li H D, Zhang Y X, Ramirez R A, Wang C, An S H, Liu S T and Wong W H 2010 A breast phantom lesion study with the high resolution transformable HOTPET camera *IEEE Trans. Nucl. Sci.* **57** 2504–9
Barrett H H, Hunter W C J, Miller B W, Moore S K, Chen Y C and Furenlid L R 2009 Maximum-likelihood methods for processing signals from gamma-ray detectors *IEEE Trans. Nucl. Sci.* **56** 725–35
Beekman F J 2009 Gamma radiation imaging apparatus EP2310876B1 (Milabs B.V.)
Beekman F J 2015 Gamma radiation breast imaging apparatus US9168014B2 (Milabs B.V.)
Berg W A 2009 Tailored supplemental screening for breast cancer: what now and what next? *AJR Am. J. Roentgenol.* **192** 390–9
Boyd N F *et al* 2007 Mammographic density and the risk and detection of breast cancer *N. Engl. J. Med.* **356** 227–36
Branderhorst W, Vastenhouw B, van der Have F, Blezer E L A, Bleeker W K and Beekman F J 2011 Targeted multi-pinhole SPECT *Eur. J. Nucl. Med. Mol. Imaging* **38** 552–61
Brzymialkiewicz C N, Tornai M P, Mckinley R L and Bowsher J E 2005 Evaluation of fully 3-D emission mammotomography with a compact cadmium zinc telluride detector *IEEE Trans. Med. Imaging* **24** 868–77
Calonge N *et al* 2010 Screening for breast cancer: U.S. preventive services task force recommendation statement (vol 151, pg 1716, 2009) *Ann. Intern. Med.* **152** 199–200
Deken M M, Bos D L, Tummers W, March T L, van de Velde C J H, Rijpkema M and Vahrmeijer A L 2019 Multimodal image-guided surgery of HER2-positive breast cancer using [(111)In]In-DTPA-trastuzumab-IRDye800CW in an orthotopic breast tumor model *EJNMMI Res.* **9** 98
Elvas F, Vangestel C, Rapic S, Verhaeghe J, Gray B, Pak K, Stroobants S, Staelens S and Wyffels L 2015 Characterization of [Tc-99m]Duramycin as a SPECT imaging agent for early assessment of tumor apoptosis *Mol. Imaging Biol.* **17** 838–47
Ferlay J, Soerjomataram I, Dikshit R, Eser S, Mathers C, Rebelo M, Parkin D M, Forman D and Bray F 2015 Cancer incidence and mortality worldwide: sources, methods and major patterns in GLOBOCAN 2012 *Int. J. Cancer* **136** E359–86
Gilland D R, Welch B L, Lee S, Kross B and Weisenberger A G 2017 Evaluation of a novel collimator for molecular breast tomosynthesis *Med. Phys.* **44** 5740–8
Gong Z Y and Williams M B 2015 Comparison of breast specific gamma imaging and molecular breast tomosynthesis in breast cancer detection: evaluation in phantoms *Med. Phys.* **42** 4250–9
Goorden M C, van Roosmalen J, van der Have F and Beekman F J 2016 Optimizing modelling in iterative image reconstruction for preclinical pinhole PET *Phys. Med. Biol.* **61** 3712–33
Hendrick R E 2010 Radiation doses and cancer risks from breast imaging studies *Radiology* **257** 246–53
Hruska C B 2017 Molecular breast imaging for screening in dense breasts: state of the art and future directions *Am. J. Roentgenol.* **208** 275–83
Hruska C B and O'Connor M K 2008a Quantification of lesion size, depth, and uptake using a dual-head molecular breast imaging system *Med. Phys.* **35** 1365–76
Hruska C B and O'Connor M K 2013 Nuclear imaging of the breast: translating achievements in instrumentation into clinical use *Med. Phys.* **40** 050901
Hruska C B, Phillips S W, Whaley D H, Rhodes D J and O'Connor M K 2008b Molecular breast imaging: use of a dual-head dedicated gamma camera to detect small breast tumors *Am. J. Roentgenol.* **191** 1805–15
Hruska C B, Weinmann A L and O'Connor M K 2012a Proof of concept for low-dose molecular breast imaging with a dual-head CZT gamma camera. Part I. Evaluation in phantoms *Med. Phys.* **39** 3466–75
Hruska C B, Weinmann A L, Skjerseth C M T, Wagenaar E M, Conners A L, Tortorelli C L, Maxwell R W, Rhodes D J and O'Connor M K 2012b Proof of concept for low-dose molecular breast imaging with a dual-head CZT gamma camera. Part II. Evaluation in patients *Med. Phys.* **39** 3476–83
Josefsson A, Nedrow J R, Park S, Banerjee S R, Rittenbach A, Jammes F, Tsui B and Sgouros G 2016 Imaging, biodistribution, and dosimetry of radionuclide-labeled PD-L1 antibody in an immunocompetent mouse model of breast cancer *Cancer Res.* **76** 472–9
Kuhn K J, Rapelyea J A, Torrente J, Teal C B and Brem R F 2016 Comparative diagnostic utility of low-dose breast-specific gamma imaging to current clinical standard *Breast J.* **22** 180–8
Long Z, Conners A L, Hunt K N, Hruska C B and O'Connor M K 2016 Performance characteristics of dedicated molecular breast imaging systems at low doses *Med. Phys.* **43** 3062–70
Macdonald L, Edwards J, Lewellen T, Haseley D, Rogers J and Kinahan P 2009 Clinical imaging characteristics of the positron emission mammography camera: PEM Flex Solo II *J. Nucl. Med.* **50** 1666–75
Mann S D, Perez K L, Mccracken E K E, Shah J P, Wong T Z and Tornai M P 2012 Initial in vivo quantification of Tc-99m sestamibi uptake as a function of tissue type in healthy breasts using dedicated breast SPECT-CT *J. Oncol.* https://doi.org/10.1155/2012/146943
Maublant J *et al* 1996 Technetium-99m-sestamibi uptake in breast tumor and associated lymph nodes *J. Nucl. Med.* **37** 922–5
Moliner L *et al* 2012 Design and evaluation of the MAMMI dedicated breast PET *Med. Phys.* **39** 5393–404
Nuyts J, Baete K, Beque D and Dupont P 2005 Comparison between MAP and postprocessed ML for image reconstruction in emission tomography when anatomical knowledge is available *IEEE Trans. Med. Imaging* **24** 667–75
O'Connor M K, Morrow M M B, Hunt K N, Boughey J C, Wahner-Roedler D L, Conners A L, Rhodes D J and Hruska C B 2017 Comparison of Tc-99m maraciclatide and Tc-99m sestamibi molecular breast imaging in patients with suspected breast cancer *EJNMMI Res.* **7**
Ogawa K, Harata Y, Ichihara T, Kubo A and Hashimoto S 1991 A practical method for position-dependent compton-scatter correction in single photon-emission CT *IEEE Trans. Med. Imaging* **10** 408–12
Rechtman L R, Lenihan M J, Lieberman J H, Teal C B, Torrente J, Rapelyea J A and Brem R F 2014 Breast-specific gamma imaging for the detection of breast cancer in dense versus nondense breasts *AJR Am. J. Roentgenol.* **202** 293–8
Rhodes D J, Hruska C B, Conners A L, Tortorelli C L, Maxwell R W, Jones K N, Toledano A Y and O'Connor M K 2015 Molecular breast imaging at reduced radiation dose for supplemental screening in mammographically dense breasts *Am. J. Roentgenol.* **204** 241–51

Rose A 1948 The sensitivity performance of the human eye on an absolute scale *J. Opt. Soc. Am.* **38** 196–208
Russo P, Larobina M, Di Lillo F, Del Vecchio S and Mettivier G J 2016 Combined SPECT/CT and PET/CT for breast imaging *Nucl. Instrum. Methods Phys. Res.* A **809** 58–66
Shepp L A and Vardi Y 1982 Maximum likelihood reconstruction for emission tomography *IEEE Trans. Med. Imaging* **1** 113–22
Shermis R B, Wilson K D, Doyle M T, Martin T S, Merryman D, Kudrolli H and Brenner R J 2016 Supplemental breast cancer screening with molecular breast imaging for women with dense breast tissue *AJR Am. J. Roentgenol.* **207** 450–7
Siman W and Kappadath S C 2012 Performance characteristics of a new pixelated portable gamma camera *Med. Phys.* **39** 3435–44
Solomon V R, Alizadeh E, Bernhard W, Hartimath S V, Hill W, Chekol R, Barreto K M, Geyer C R and Fonge H 2019 (111)In- and (225)Ac-labeled cixutumumab for imaging and alpha-particle radiotherapy of IGF-1R positive triple-negative breast cancer *Mol. Pharm.* **16** 4807–16
Spanu A, Sanna D, Chessa F, Farris A, Nuvoli S and Madeddu G 2011 The usefulness of Tc-99m-tetrofosmin SPECT/CT in the detection of residual tumors and axillary lymph node metastases in breast cancer patients following neoadjuvant therapy *Clin. Nucl. Med.* **36** 997–1002
Specht J M and Mankoff D A 2012 Advances in molecular imaging for breast cancer detection and characterization *Breast Cancer Res.* **14**
van der Have F, Vastenhouw B, Rentmeester M and Beekman F J 2008 System calibration and statistical image reconstruction for ultra-high resolution stationary pinhole SPECT *IEEE Trans. Med. Imaging* **27** 960–71
van Roosmalen J, Beekman F J and Goorden M C 2017 System geometry optimization for molecular breast tomosynthesis with focusing multi-pinhole collimators *Phys. Med. Biol.* **63** 015018
van Roosmalen J, Beekman F J and Goorden M C 2018 Comparison of fan beam, slit-slat and multi-pinhole collimators for molecular breast tomosynthesis *Phys. Med. Biol.* **63** 105009
van Roosmalen J, Goorden M C and Beekman F J 2016 Molecular breast tomosynthesis with scanning focus multi-pinhole cameras *Phys. Med. Biol.* **61** 5508
Velikina J, Leng S and Chen G H 2007 Limited view angle tomographic image reconstruction via total variation minimization *Med. Imaging 2007 Phys. Med. Imaging* **6510** 1–3
Wang B, Kreuger R, Beekman F J and Goorden M C 2018 Novel light-guide-PMT geometries to reduce dead edges of a scintillation camera *Phys. Medica.* **48** 84–90
Wang B, Kreuger R, Huizenga J, Beekman F J and Goorden M C 2019 Experimental validation of a gamma detector with a novel light-guide-PMT geometry to reduce dead edge effects *IEEE Trans. Radiat. Plasma Med. Sci.* **4** 98–107
Wang B, van Roosmalen J, Piët L, van Schie M A, Beekman F J and Goorden M G 2017 Voxelized ray-tracing simulation dedicated to multi-pinhole molecular breast tomosynthesis *Biomed. Phys. Eng. Expr.* **3** 045021
Yaffe M J 2008 Mammographic density. Measurement of mammographic density *Breast Cancer Res.* **10** 209
Yanagida T *et al* 2010 Development of Pr:LuAG scintillator array and assembly for positron emission mammography *IEEE Trans. Nucl. Sci.* **57** 1492–5
Zhou Y, Shao G and Liu S 2012 Monitoring Breast Tumor Lung Metastasis by U-SPECT-II/CT with an Integrin alpha(v)beta(3)-Targeted Radiotracer(99m)Tc-3P-RGD(2) *Theranostics* **2** 577–88